ADVANCED FUNCTIONAL MATERIALS
www.afm-journal.de

# Morphological and Electrochemical Cycling Effects in $MnO_2$ Nanostructures by 3D Electron Tomography

*Wei Chen, Raghavan B. Rakhi, Qingxiao Wang, Mohamed N. Hedhili, and Husam N. Alshareef**

**In this study, $MnO_2$ nanostructures with well-controlled morphology and crystal phase are successfully prepared by chemical synthesis, and characterized by three-dimensional electron tomography for use as supercapacitor electrode materials. The growth process of the various $MnO_2$ nanostructures is revealed in detail, and correlated to their electrochemical performance as supercapacitor materials. The specific capacitance of $MnO_2$ electrodes is found to be strongly correlated with the inner morphology and crystal phase of the $MnO_2$ nanostructures. Furthermore, it is demonstrated that the increased capacity with electrochemical cycling of the materials is due to the formation of defective regions embedded in the $MnO_2$ nanostructures; these regions form during electrochemical cycling of the electrodes, resulting in increased porosity, surface area, and consequently, increased electrochemical capacity.**

## 1. Introduction

Manganese dioxide ($MnO_2$) is considered to be one of the most promising materials for energy storage systems including batteries and supercapacitors.[1–5] Owing to its many good features of low cost, high theoretical capacity, environmental friendliness and natural abundance, $MnO_2$ has been extensively investigated as an electrode material for high performance supercapacitors.[5] Compared to batteries, supercapacitors have much higher power density (10–100 times higher than batteries), fast charge rate (charge a supercapacitor takes only a few seconds to minutes) and excellent cycling stability (cycle number of more than 1 million cycles). This makes supercapacitors ideal devices for many critical applications such as consumer electronics, hybrid electric vehicles, and smart grid storage.[6,7] However, their relatively lower energy density (~10 times lower than that of batteries) has thus far limited their wide-spread application as energy storage devices.[8] Carbon-based supercapacitors show low charge storage capacity due to the limited electrolyte ions adsorption and desorption on the surface of the carbon. Therefore, replacing carbon materials in commercial supercapacitors by high capacity materials like $MnO_2$ can be an effective strategy to increase the energy density of supercapacitors, thus paving the way for their adoption in a variety of applications. However, oxide electrodes have the fatal disadvantage of poor cycling performance, an issue that so far has not been sufficiently investigated.

Various methods have been used to prepare $MnO_2$ nanostructures such as sol-gel, co-precipitation, hydrothermal reaction, and electrochemical deposition.[9–14] Additionally, a large variety of $MnO_2$ with different morphologies (such as nanoparticles, nanocubes, nanorods, nanotubes) and different crystalline phases (such as $\alpha$, $\beta$, $\gamma$, $\varepsilon$, $\delta$) have been produced.[15–20] However, a systematic study focused on studying the effect of $MnO_2$ nanoscale morphology and crystal phase and its cycling performance on supercapacitor capacity has not been performed. One of the very first studies conducted by Belanger et al. revealed the energy storage mechanism of $MnO_2$ electrode in aqueous electrolyte by cyclic voltammetry and X-ray photoelectron spectroscopy techniques.[21] They found that the $MnO_2$ electrode with thick layer underwent no change of the Mn oxidation state because only a very thin layer of the material contributed to the energy storage process.[21] Afterwards, Wei et al. carried out a study of the influence of $MnO_2$ morphology on the electrochemical properties by controlling the material synthesis conditions.[22] The electrochemical tests demonstrated that the storage capacity of $MnO_2$ electrodes is highly related to its morphology, nanostructure, and surface area, but the study did not provide very detailed material analysis to elucidate the factors that control electrochemical performance of the devices.[22] In order to achieve the best energy storage performance of $MnO_2$ and better understand the energy storage mechanism, it is very important to study not only the general shape or nanostructure of $MnO_2$ but also the evolution of the nanostructures with electrochemical cycling to the supercapacitor performance.

We report here a comprehensive study on investigating the energy storage mechanism of nanostructured $MnO_2$ by a systematic route using multiple techniques that some of them have rarely been utilized to study $MnO_2$ based supercapacitors previously. Firstly, we prepared different $MnO_2$ nanostructures with well-controlled morphology and crystallinity by a facile hydrothermal reaction. In addition to many conventional

---

W. Chen, Dr. R. B. Rakhi, Prof. H. N. Alshareef
Materials Science and Engineering
King Abdullah University of Science
and Technology (KAUST)
Thuwal, 23955-6900, Saudi Arabia
E-mail: husam.alshareef@kaust.edu.sa
Q. Wang, Dr. M. N. Hedhili
Advanced Imaging and Characterization Laboratory, KAUST
Thuwal, 23955-6900, Saudi Arabia

DOI: 10.1002/adfm.201303508

characterization methods, three-dimensional scanning transmission electron microscopy tomography was used, for the first time, to explain the growth of the $MnO_2$ and the corresponding cycling performance of the supercapacitors. Furthermore, the electrochemical performance of the $MnO_2$ nanostructures was studied in detail and we enriched the energy storage mechanism of $MnO_2$ by direct observation of the evolution of material structure during long-term cycling tests.

## 2. Results and Discussion

### 2.1. General Characterization of $MnO_2$ Nanostructures

Different morphologies of $MnO_2$ nanostructures were prepared by a hydrothermal reaction between $KMnO_4$ and HCl in aqueous solution. The reaction periods were chosen to engineer the morphology of the $MnO_2$ electrodes, and included reaction times of 1 h, 1.5 h, 2 h, 4 h, 8 h and 12 h. As shown in **Figure 1**, after a reaction of 1 h, the mixed solution of $KMnO_4$ and HCl aqueous medium results in the nucleation and growth of porous nanospheres (inset in Figure 1a). The nanospheres are comprised of many wrinkled nanosheets, which are self-assembled perpendicular to the outer surface of the nanospheres (Figure 1a). The porous nanospheres have typical diameters ranging from a few hundred nanometers to several micrometers, and the gaps between the nanosheets vary from 50 nm to 300 nm. When the reaction time is increased to 1.5 h, short nanofibers begin to emerge between the nanosheets, as marked by the red arrows in Figure 1b. However, the porous sphere-like morphology persists, and the nanosheets are still dominant over nanofibers. When the hydrothermal reaction is further prolonged to 2 h (Figure 1c), more nanofibers grow from the nanosheets and the diameter of the nanofibers also increases, compared to the sample in Figure 1b. It is interesting to note that the nanosheets inside the nanospheres disappear completely when the reaction time extends to 4 h (Figure 1d), and instead of forming more nanofibers, a large number of nanotubes are formed. The nanotubes formation can be seen from their end tips (Figure 1d), and will be confirmed later in the paper. The nanotubes replace the original nanosheets, but the overall sphere-like morphology is retained, where each nanosphere consists of $MnO_2$ nanotube bundles. When the reaction time reaches 8 h (Figure 1e), the nanotubes still exist but the overall morphology of $MnO_2$ has changed to hollow urchin-like structure, which is less agglomerated as compared to the morphology in Figure 1d. Finally, after reaction time of 12 h, the individual nanotubes disperse well in the reaction solution and the nanosphere morphology disappears (Figure 1f).

X-ray diffraction (XRD) was carried out to investigate the crystal structure and phase purity of the as-prepared $MnO_2$ nanostructures with different morphologies. It is found that the $MnO_2$ can be classified into two different crystalline structures, depending on the hydrothermal reaction time. When the hydrothermal reaction is less than 2 h, the diffraction peaks of the $MnO_2$ shown in **Figure 2** can be indexed to K-Birnessite $\delta$-$MnO_2$ (JCPDS 01-080-1098, base-centered monoclinic with a = 5.149 Å, b = 2.843 Å, c = 7.176 Å and $\beta$ = 100.76°).[23] The broad and low intensity XRD peaks indicate a poor or

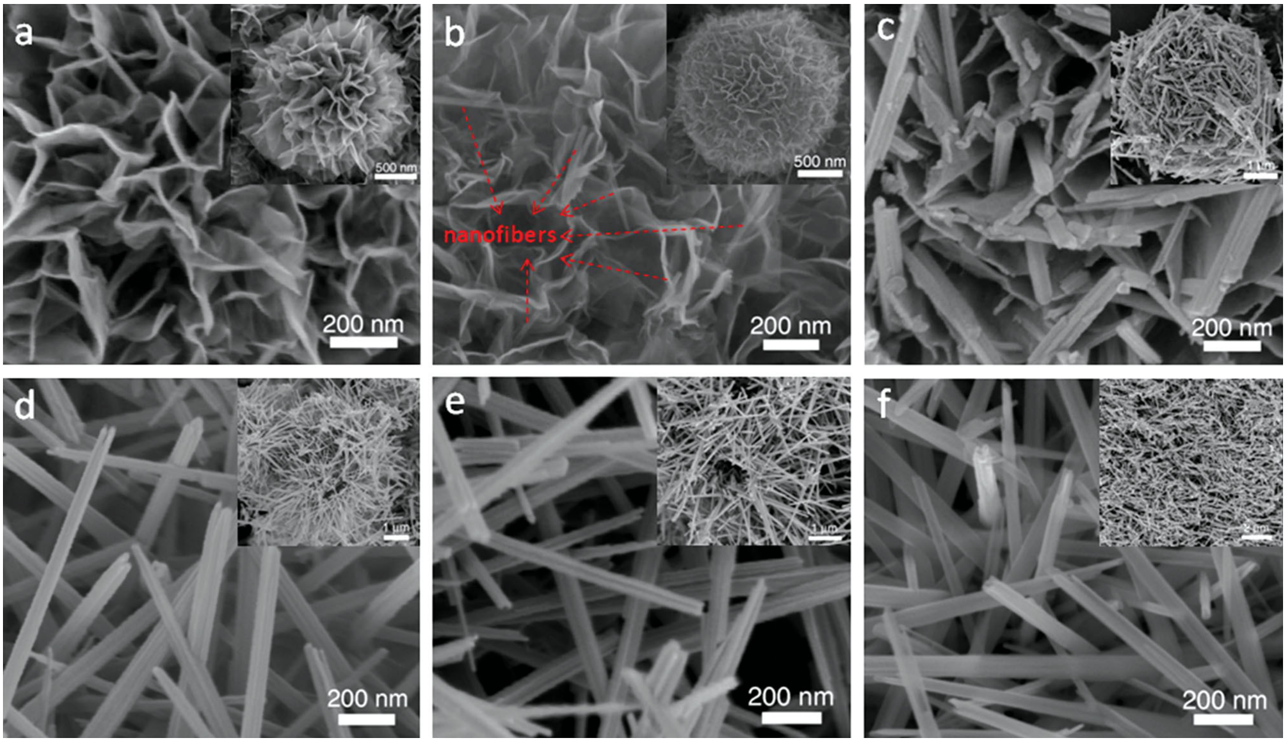

**Figure 1.** Scanning electron microscope (SEM) images of the $MnO_2$ nanostructures obtained at different hydrothermal reaction times. (a) $MnO_2$-1 h; (b) 1.5 h; (c) 2 h; (d) 4 h; (e) 8 h; (f) 12 h.

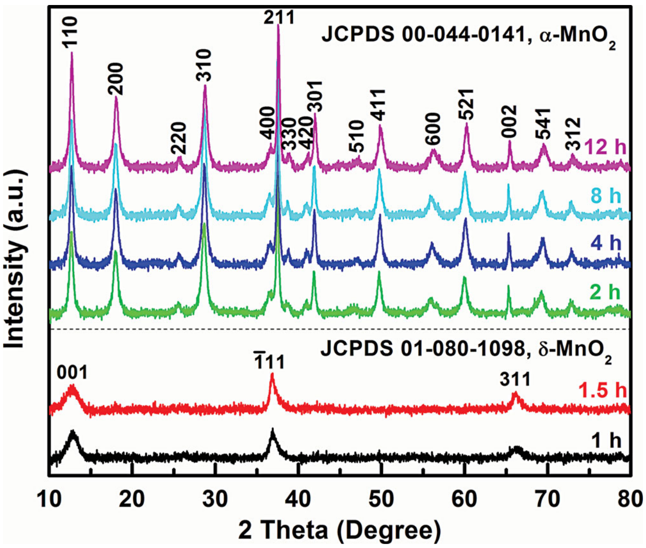

**Figure 2.** XRD patterns of the $MnO_2$ nanostructures obtained at different hydrothermal reaction times, ranged from 1 h to 12 h.

polycrystalline feature of the layered $\delta$-$MnO_2$. While for the $MnO_2$ obtained at hydrothermal reaction of more than 2 h, the sharp and high intensity peaks correspond to $\alpha$-$MnO_2$ (JCPDS 00-044-0141, body-centered tetragonal with a = 9.78 Å and c = 2.86 Å), indicating the high crystallinity and high purity of the $MnO_2$ prepared by the facile hydrothermal method.[24] Therefore, the crystal phase and morphology of the $MnO_2$ nanostructures can be controlled very well by the reaction time.

Transmission electron microscopy (TEM) was used to characterize the interior of the $MnO_2$ nanostructures with different morphologies. **Figure 3**a shows folded $MnO_2$ nanosheets that self-assembled into porous nanospheres (inset of Figure 3a), corresponding to the $MnO_2$ morphology observed in the SEM in Figure 1a. Furthermore, the TEM images in Figure 3b confirm that the nanofibers start to appear from the surface of the nanosheets within the nanospheres, as was demonstrated by the SEM in Figure 1b. It is also observed in Figure 3b that the nanofibers are polycrystalline. The lattice fringes show d-spacings of 0.24 nm and 0.31 nm, corresponding to the d values of (211) and (310) planes of $\alpha$-$MnO_2$, respectively. This indicates that the $\delta$-$MnO_2$ nanosheets convert to polycrystalline $\alpha$-$MnO_2$ nanofibers in the initial phase of nanofiber formation. This result is further confirmed by another HRTEM image captured on the edge of the nanosphere and shown in the supporting information Figure S1. Rod-like nanoparticles with different orientations are formed from the nanosheets. The lattice fringe with spacing of 0.49 nm corresponds to d value of (200) plane of $\alpha$-$MnO_2$. Figure 3c shows the TEM image of $MnO_2$ nanostructure formed at a 2 h hydrothermal reaction time. The overall morphology in the inset of Figure 3c shows that the nanospheres are composed of a number of nanofibers. Enlarged image of the selected region in Figure 3c

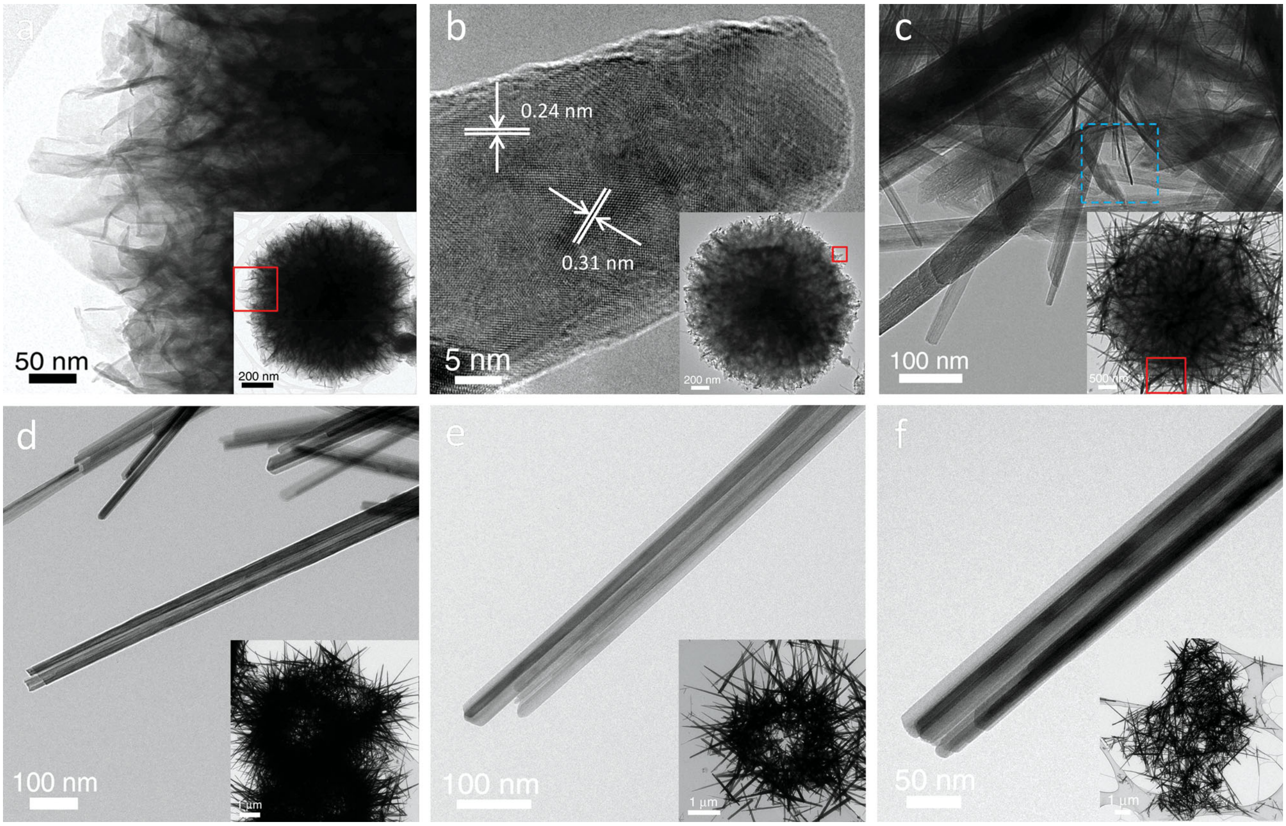

**Figure 3.** TEM images of the $MnO_2$ nanostructures obtained at different hydrothermal reaction times. (a) $MnO_2$-1 h; (b) 1.5 h; (c) 2 h; (d) 4 h; (e) 8 h; (f) 12 h.

**Table 1.** The summary of $MnO_2$ nanostructures in terms of morphology, crystallinity and BET surface area.

| Reaction time [h] | 1 | 1.5 | 2 | 4 | 8 | 12 |
|---|---|---|---|---|---|---|
| Morphology | spheres consisting of sheets | sheets + fibers | sheets (less) + fibers (more) | tubes | tubes | tubes |
| Crystallinity | poly-crystalline $\delta$-$MnO_2$ sheets | polycrystalline $\delta$-$MnO_2$ sheets and polycrystalline $\alpha$-$MnO_2$ fibers | polycrystalline $\delta$-$MnO_2$ sheets and polycrystalline $\alpha$-$MnO_2$ fibers | single crystalline $\alpha$-$MnO_2$ tubes | single crystalline $\alpha$-$MnO_2$ tubes | single crystalline $\alpha$-$MnO_2$ tubes |
| BET surface area [$m^2$/g] | 201.65 | 156.35 | 55.62 | 44.99 | 41.58 | 40.58 |

inset (marked by the red square) exhibits the coexistence of $MnO_2$ nanosheets and nanofibers, which agrees well with the morphology observed by SEM in Figure 1c. The nanofibers have their one end embedded in the nanosheets, indicating that the growth of $MnO_2$ nanofibers originates from the nanosheets.[19] HRTEM (high resolution TEM) image of the $MnO_2$-2 h sample (Figure S2, the area enclosed by the blue rectangular in Figure 3c) shows the coexistence of $\delta$-$MnO_2$ and $\alpha$-$MnO_2$, as confirmed by the d-spacing of 0.7 nm ((001) plane of $\delta$-$MnO_2$) and 0.49 nm ((200) plane $\alpha$-$MnO_2$) respectively. Figure 3d shows the hollow urchin-like $MnO_2$ sphere, consisting of a bundle of nanotubes obtained at reaction time of 4 h. Most of the nanotubes in this stage are not completely hollow tubes, with only the outer end part of the tubes becoming hollow (Figure 3d). However, the end tips of the $MnO_2$ nanotubes have become rough and irregular, different from the smooth and neat shape of the nanofibers (Figure 3b). The tubular morphology of individual $MnO_2$ remained with increasing reaction time, as shown in Figure 3e (reaction time of 8 h) and Figure 3f (reaction time of 12 h). However, at these long reaction times (8 and 12 h), the overall morphology of $MnO_2$ evolved to rather hollow spheres (Inset of Figure 3e) and well-dispersed nanotubes (Inset of Figure 3f). The evolution of the $MnO_2$ nanostructure and morphology is summarized in **Table 1**.

Additional HRTEM and selected area electron diffraction (SAED) were performed on $MnO_2$. **Figure 4**a shows a folded nanosheet in one of the $MnO_2$ nanospheres. By careful inspection, it can be seen that the nanosheet consists of many small domains with different orientations, confirming its polycrystalline nature. The observed fringes with spacing of 0.7 nm and 0.24 nm correspond to the d value of (001) and $(\bar{1}11)$ planes of $\delta$-$MnO_2$. The SAED pattern taken in approximately the same region as Figure 4a displays two characteristic rings that correspond to (311) and $(\bar{1}11)$ planes of $\delta$-$MnO_2$ (Figure 4b). The appearance of (311) plane in the SAED pattern is not observed in the HRTEM image due to the limited spatial resolution of the TEM. Nevertheless, the HRTEM together with its SAED pattern confirm that the $MnO_2$ nanospheres are $\delta$-$MnO_2$ with polycrystalline nature for short hydrothermal reaction time (1 h). In contrast, the $MnO_2$ nanotubes formed after long hydrothermal reaction time (12 h) demonstrate the typical hollow structure with irregular open tips (Figure 4c). The highly crystalline lattice fringes in the HRTEM image (Figure 4c) indicate the single crystalline characteristic of the $MnO_2$ nanotubes, as confirmed by the corresponding SAED pattern (inset of Figure 4c). The growth direction of the nanotubes is [001], which can be determined from its SAED pattern and further confirmed by the cross-sectional TEM image of $MnO_2$ nanotube and its corresponding SAED pattern (Figure 4d).

### 2.2. 3D Electron Tomography of $MnO_2$

Although the morphological and crystalline characteristics of $MnO_2$ nanostructures can be identified from 2D TEM images, some important information on the material may still be difficult to detect due to the limitation of 2D projection in the TEM technique.[25] We therefore adopted 3D electron tomography to visualize the 3D morphological evolution of the various 1D $MnO_2$ nanostructures to better understand the growth process and the corresponding electrochemical performance of $MnO_2$ electrodes.[26] Three different morphologies of the 1D $MnO_2$ were selected for study using 3D electron tomography: (i) nanofibers obtained at hydrothermal reaction time of 2 h, nanotubes obtained at hydrothermal reaction time of (ii) 4 h, and (iii) 12 h. We understand that it is difficult to cover all the different morphologies, but the selected three morphologies are enough to show the evolution of the 1D $MnO_2$ nanostructures. As depicted in **Figure 5**, the reconstructed 3D images and their cross sectional slices exhibit the overall morphology and interior structure of $MnO_2$, information that is not available by conventional TEM images, but is extremely important to explain the growth process and electrochemical performance of $MnO_2$. Take the $MnO_2$ nanofiber ($MnO_2$-2 h) as an exampleV, the constructed 3D image in Figure 5a shows a nanofiber with smooth outer surface. Figure 5b shows that the inside of the nanofiber is completely solid without any voids or defects. However, some areas on the tip of the nanofiber are rough, as illustrated by the red circles in Figure 5a and b. This roughness is probably caused by the acid etching effect in the reaction solution, indicating that the etching process preferably takes place on side surfaces of the nanofibers. The cross-sectional slice shown in Figure 5c is irregularly shaped indicating that one side of the outer surface is also corroded slightly by the acid etching. The corresponding 3D representation of the nanofibers is available in Movie S1 and S2 in the Supporting Information. The perpendicular projections of the two ends of the nanofibers are also displayed in Figure S3a and b, together with the semi-transparent 3D reconstruction (Figure S3c) and a cross-sectional slice taken at another site along the nanofiber (Figure S3d). All this information confirms the solid interior of the nanofibers. As for the $MnO_2$ nanotubes ($MnO_2$-4 h), their outer surfaces are quite rough and irregular (Figure 5d–f), which is a result of being seriously etched by the acids. The 3D reconstruction of the nanotube shows clearly the formation

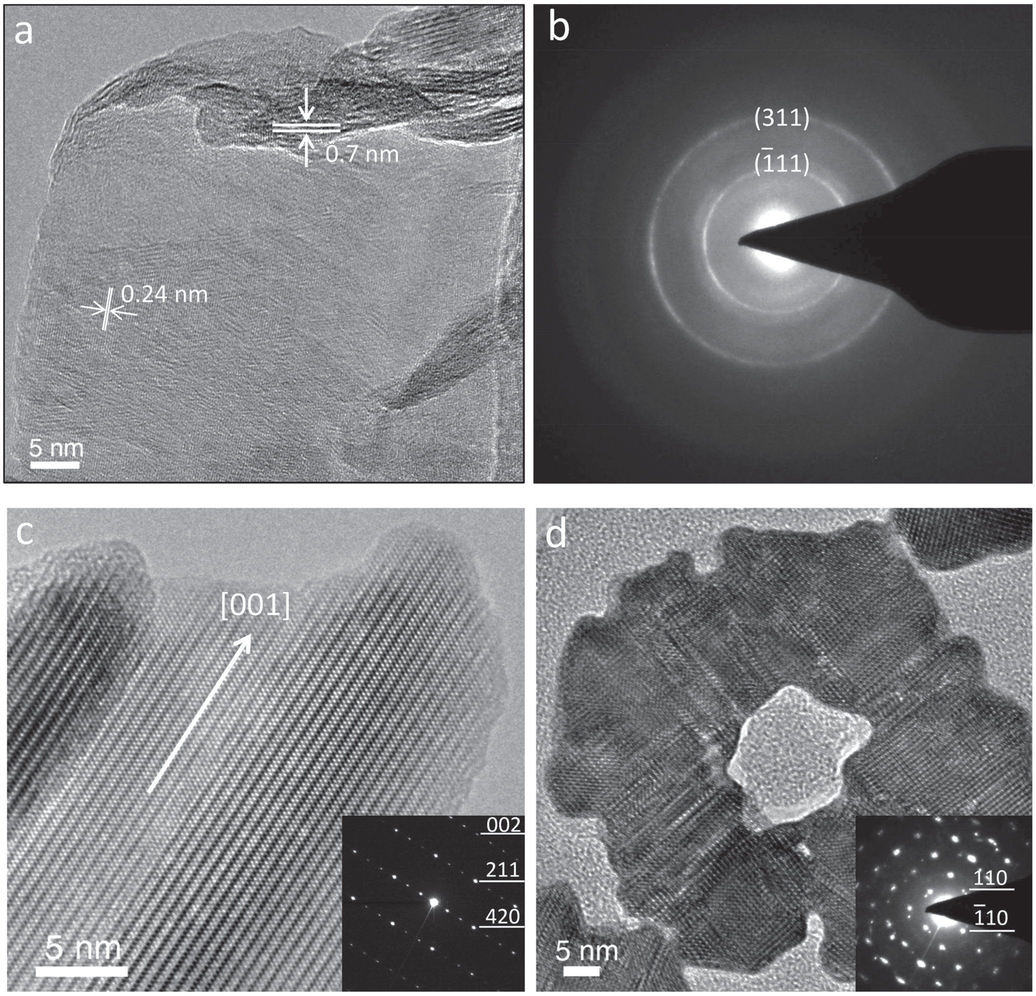

**Figure 4.** HRTEM images of (a) the $MnO_2$ nanosheet ($MnO_2$-1 h) and (b) the corresponding SAED pattern; (c) $MnO_2$ nanotube ($MnO_2$-12 h) and the corresponding SAED pattern and (d) cross-sectional TEM image with the corresponding SAED pattern ($MnO_2$-12 h).

of the voids. It is further revealed that these voids are preferable to grow laterally along the nanotubes as labeled by the red rectangles in Figure 5e, which are caused by the recrystallization during the Ostwald ripening process (discussed in the next section). The irregular nanotube was formed as a result of further growth of the central voids that run the entire length of the structure, as confirmed by the cross sectional images taken at the two ends of the nanotube (Figure S3e–h). In the case of $MnO_2$ nanotubes obtained at a reaction time of 12 h ($MnO_2$-12 h), the outer surface of the structure has been further corroded by the acid etching process, forming larger hollow openings and even rupturing the walls of the nanotubes, as indicated by the red arrows in Figure 5g and h. It is a combined result that dominated by the ripening and etching processes (Figure i, Figure S3i–l). The 3D representations of these highly corroded nanotubes ($MnO_2$-4 h and –12 h) are also available in Movies S3&4 and S5&6 in the Supporting Information.

### 2.3. Growth Process of the $MnO_2$ Nanostructures

In order to get the desired morphology and crystal phase for specific applications, it is important to understand the growth process of the $MnO_2$ nanostructures. Several growth mechanisms of the hydrothermally synthesized $MnO_2$ have been proposed in the previous reports. Wang *et al.* proposed a rolling mechanism to explain the formation of one-dimensional $MnO_2$ from lamellar structure of $MnO_2$.[27] Luo *et al.* suggested that the formation of $MnO_2$ nanotube is a result of the acid etching process in the reaction solution.[24] Recently, Li *et al.* provided an “oriented attachment” mechanism to illustrate the conversion of $MnO_2$ nanotubes from nanorods.[28] Truong *et al.* proposed the diffusion of nanosheets and the anisotropic growth of nanowires, followed by an Ostwald ripening process to form $MnO_2$ nanotubes.[19] Taking the 3D reconstruction of the nanostructures by electron tomography and combining with the results obtained from XRD, SEM and TEM, we are able to provide vivid insight into the internal nanostructure evolution during the hydrothermal growth process of $MnO_2$.[26] **Figure 6** summarizes our view of the growth process of $MnO_2$ nanostructures. As shown in Figure 6a, the rose-like $MnO_2$ nanoflower consists of numerous nanosheets that form after a short reaction time once the reaction solution has reached the target temperature. The observation of this very first step in our experiment agrees well with the previous reports.[16,19] The

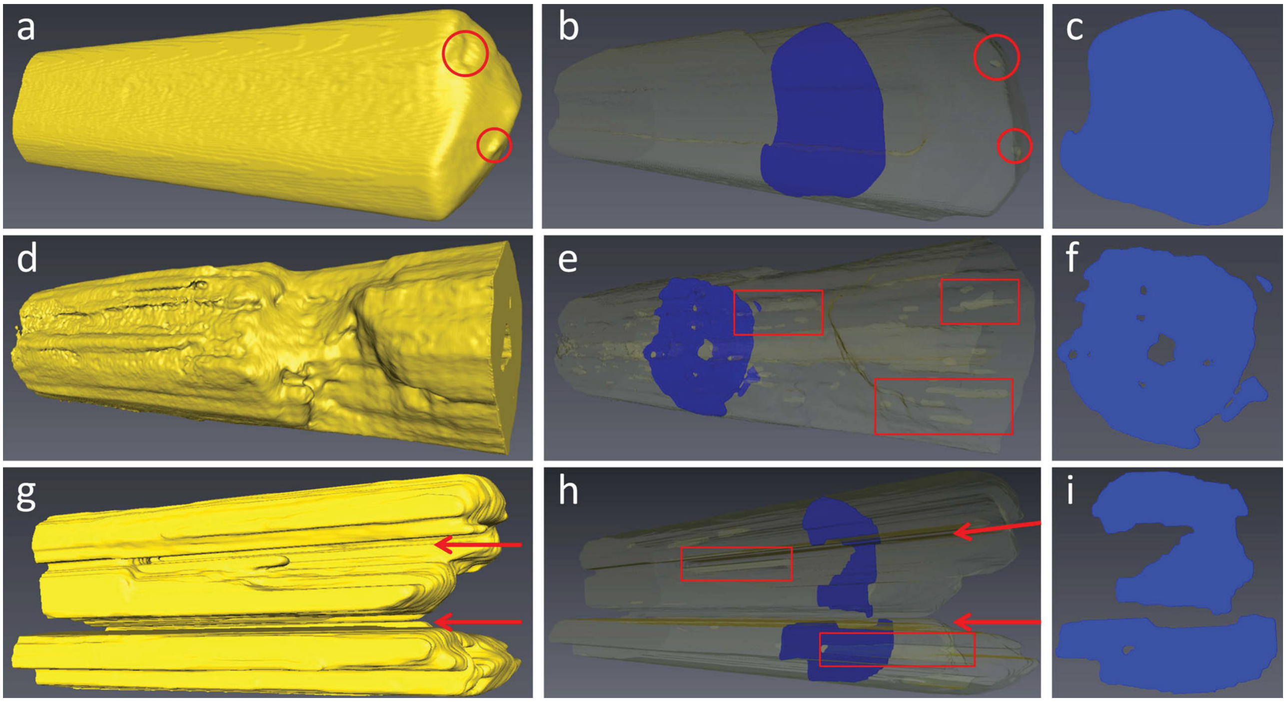

**Figure 5.** 3D electron tomography of 1D $MnO_2$ nanostructures. 3D reconstruction, semi-transparent reconstruction and the cross sectional slice for (a–c) $MnO_2$ nanofiber ($MnO_2$-2 h), (d–f) $MnO_2$ nanotube ($MnO_2$-4 h), (g–i) $MnO_2$ nanotube ($MnO_2$-12 h), respectively.

formation of the $MnO_2$ nanospheres is probably a result of the following reactions:

$$2MnO_4^- + 8H^+ + 6Cl^- \rightarrow 2MnO_2 + 3Cl_2 + 4H_2O \quad (1)$$

$$4MnO_4^- + 4H^+ \rightarrow 4MnO_2 + 3O_2 + 2H_2O \quad (2)$$

The $MnO_2$ nanosheets are determined to be $\delta$-$MnO_2$, as revealed by XRD and TEM, which is a layered structure composed of edge-shared $MnO_6$ octahedral units.[27] However, the layered $\delta$-$MnO_2$ nanosheets are in a metastable state and tend to be diffused to stable $\alpha$-$MnO_2$ at elevated temperature and pressure, resulting in the conversion from nanosheets to nanofibers as illustrated in Figure 6b. The short nanofibers inherit the polycrystalline nature of the nanosheets of $MnO_2$, but their crystalline phase changes from $\delta$-$MnO_2$ to $\alpha$-$MnO_2$ as the $MnO_2$ one-dimensional structures is formed. This phase change is driven by an overall reduction of the free energy of the system as the $\alpha$-$MnO_2$ is a 2 × 2 tunneled structure with higher crystallinity, and is thermodynamically more stable than the $\delta$-$MnO_2$.[17,28] These observations agree with the growth mechanism that has been proposed by Truong et al. for the formation of 1D nanostructures from 2D nanosheets.[19] With increasing the reaction time, more energy is introduced into the system. The $\delta$-$MnO_2$ nanosheets continue to diffuse until completely consumed while the $\alpha$-$MnO_2$ nanofibers continue to grow, finally resulting in $\alpha$-$MnO_2$ nanofibers (Inset of Figure 6c). In the meantime, some of the $\alpha$-$MnO_2$ nanofibers start to undergo an Ostwald ripening process that converts the polycrystalline $\alpha$-$MnO_2$ nanofibers to single crystalline phase. Due to the direct contact of the outer surface with the reaction solution, the nanofiber outer surface can firstly become highly crystalline, while the ripening process in its interior is much slower owing to their different activities of the polycrystalline nanodomains (Figure 6c).[19] As the hydrothermal reaction time is further increased, the conversion of nanosheets to nanofibers is completed and some partially hollow nanotubes are formed (Figure 6d). The formation of nanotubes from nanofibers was confirmed earlier by 3D electron tomography, which is caused by the further Ostwald ripening in the interior portion of the nanofibers due to the contact of the nanofiber ends with the reaction solution. As discussed in the previous section, the nanofibers are easily converted to irregular nanotubes under the high temperature and strong acid conditions, which is dominated by the ripening process as well as the acid etching process. The effect of the acid etching process is favored on the outer surfaces of the nanofibers, because the side surfaces can access the surrounding acid more easily than the materials inside the nanofibers, inducing the concave side surfaces and even large openings that observed by the 3D electron tomography. Longer hydrothermal reaction times make the nanotubes more hollow and more crystalline, while individual nanotube starting to disperse more uniformly in the solution (Figure 6e,f), slowly losing the overall spherical/urchin-like morphology.

In summary, our detailed analysis suggests that the nucleation and growth process of the $MnO_2$ nanostructures formed by the hydrothermal reaction proceed as flows: (a) nucleation and self-assembly of $MnO_2$ nanosheets into 3D nanospheres, (b) the formation of 1D nanofibers that nucleate out of the nanosheets, and subsequent conversion of the nanosheets to short nanofibers, (c) growth of the nanofibers in size and length, along with continued conversion of nanosheets to nanofibers, (d) complete conversion of nanosheets to nanofibers, and for-

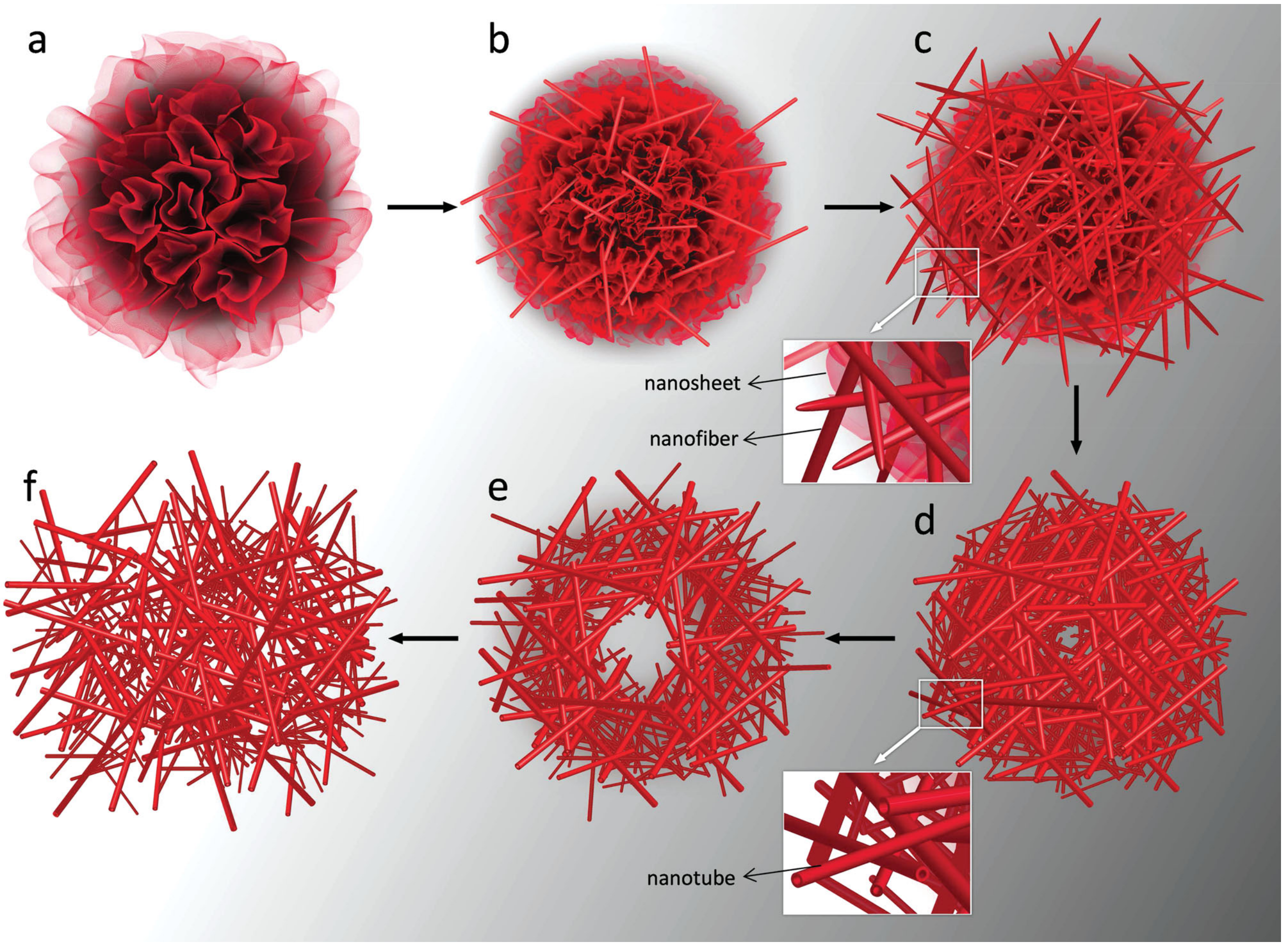

**Figure 6.** Schematic illustrations of the growth process of $MnO_2$ nanostructures controlled by the hydrothermal reaction time. (a) $MnO_2$-1 h; (b) 1.5 h; (c) 2 h; (d) 4 h; (e) 8 h; (f) 12 h.

mation of nanotubes from nanofibers, (e) continued formation of nanotubes with more hollow interior. In the meantime, the crystal phase of $MnO_2$ transforms from polycrystalline $\delta$-$MnO_2$ nanosheets to polycrystalline $\alpha$-$MnO_2$ nanofibers, and then to single crystalline $\alpha$-$MnO_2$ nanofibers and nanotubes.

### 2.4. Electrochemical Performance of $MnO_2$ Nanostructures

#### *2.4.1. Morphological Effects*

The electrochemical properties of nanostructured $MnO_2$ as electrode material for supercapacitors were studied in a three-electrode configuration by means of cyclic voltammetry (CV), galvanostatic charge-discharge (CD) and electrochemical impedance spectroscopy (EIS). The purpose of the electrochemical study is to understand the impact of the morphological variation on the energy storage mechanism of $MnO_2$. The $MnO_2$ nanostructures with different morphologies and crystal phases obtained at different hydrothermal reaction times were all systematically studied as supercapacitor electrode materials (Figure S4-9), and their electrochemical behaviors are summarized in **Figure 7**. Figure 7a and b show the CV curves at the same scan rate of 10 mV $s^{-1}$ and CD at the same current density of 1 A $g^{-1}$ for all samples before cycling tests. All CV curves show nearly rectangular shapes (Figure 7a), corresponding to the highly symmetrical charge and discharge curves (Figure 7b), which all indicate good supercapacitor characteristics that agree well with the previous reports.[29,30] At the same scan rate, the measured current density of the $MnO_2$ nanostructures decreases with the hydrothermal reaction time. This results in the decrease of area under the CV loops with the reaction time. Similarly, under the same applied current density of 1 A $g^{-1}$, the charge and discharge time becomes shorter as the hydrothermal reaction time increases, suggesting the decrease in capacitance with the reaction time. As a result, the sample of $MnO_2$-1 h shows the highest values of specific capacitance, while the sample of $MnO_2$-12 h shows the lowest ones (Figure 7c). It is worth noting that the capacitance of $MnO_2$-1.5 h is only slightly lower than that of $MnO_2$-1 h, but the values of other samples ($MnO_2$-2 h, 4 h, 8 h and 12 h) are much lower than that of $MnO_2$-1 h. The capacitances of $MnO_2$-2 h, 4 h, 8 h and 12 h are in a relatively low range between 10 F $g^{-1}$ and 30 F $g^{-1}$, while the range for $MnO_2$-1 h and 1.5 h is between 50 F $g^{-1}$ and 110 F $g^{-1}$.

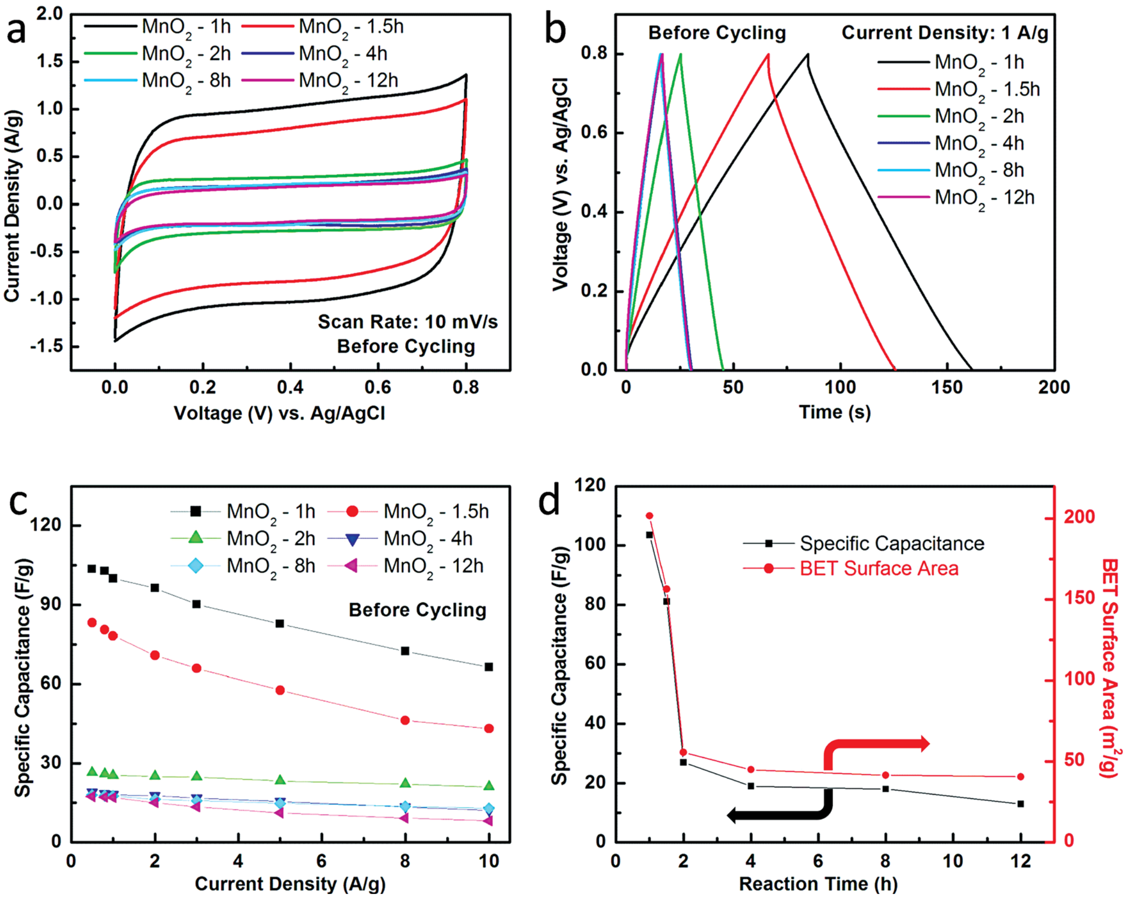

**Figure 7.** Electrochemical performance of all $MnO_2$ nanostructures as supercapacitor electrode materials before cycling tests. (a) Cyclic voltammetry at scan rate of 10 mV $s^{-1}$; (b) Galvanostatic charge-discharge at current density of 1 A $g^{-1}$; (c) Specific capacitance vs. current density; (d) The change of specific capacitance (at 0.5 A $g^{-1}$) and BET specific surface area with the reaction time.

It is known that the electrochemical performance of supercapacitive materials is highly dependent to their surface area for both electrochemical double layer storage mechanism and pseudocapacitive storage mechanism.[7] The morphological evolution of the $MnO_2$ from nanosheets to nanofibers and finally nanotubes, together with the crystallinity change from polycrystalline to single crystalline resulted in a huge difference in the surface area of the $MnO_2$ nanostructures used in this study. As shown in Figure S10, the nitrogen adsorption and desorption isotherm curves demonstrate typical type IV curves for all $MnO_2$ nanostructures, indicating the mesoporous nature of the materials. The calculated specific surface area (SSA) based on Brunauer–Emmett–Teller (BET) model for all $MnO_2$ is presented in Table 1. The SSA changes with the hydrothermal reaction time over a wide range (Figure 7d). Specifically, the SSA of the samples of $MnO_2$-1 h (201.65 $m^2$ $g^{-1}$) and $MnO_2$-1.5 h (156.35 $m^2$ $g^{-1}$) are three to four-fold higher than that of $MnO_2$-2 h (55.62 $m^2$ $g^{-1}$), $MnO_2$-4 h (44.99 $m^2$ $g^{-1}$), $MnO_2$-8 h (41.58 $m^2$ $g^{-1}$), and $MnO_2$-12 h (40.58 $m^2$ $g^{-1}$). The dramatic decrease of the SSA is caused by the conversion of $MnO_2$ nanosheets to nanofibers/nanotubes, accompanied by the transformation of poor crystalline lamellar structured $\delta$-$MnO_2$ to highly crystalline tunnel structured $\alpha$-$MnO_2$. The decrease of the SSA with the reaction time is highly correlated to the decrease of the capacitance as shown in Figure 7d, which agrees well with the reports.[31,32] Some previous studies also showed that the amorphous/poor crystalline $MnO_2$ with higher SSA is preferable as supercapacitor material.[33–35] The pore size distribution of the $MnO_2$ nanostructures (Figure S10b) shows a relatively narrow pore size distribution of the materials (average pore size between 7 and 13 nm), indicating the uniform pores of our $MnO_2$ nanostructures.

### 2.4.2. Electrochemical Cycling Effects

We then studied the electrochemical cycling effect on the performance of all the $MnO_2$ nanostructures. We pick up the sample of $MnO_2$-1 h as an example. **Figure 8** shows the electrochemical performance of $MnO_2$-1 h sample before and after 5000 cycles. The $MnO_2$-1 h electrode shows nearly rectangular CV curves after 5000 cycles (Figure 8a). The CD curves in Figure 8b show symmetrical charge-discharge behaviors, consistent with the performance of CV curves in Figure 8a. The CV curves at different scan rates and CD under different current densities of the $MnO_2$-1 h sample before and after 5000 cycles

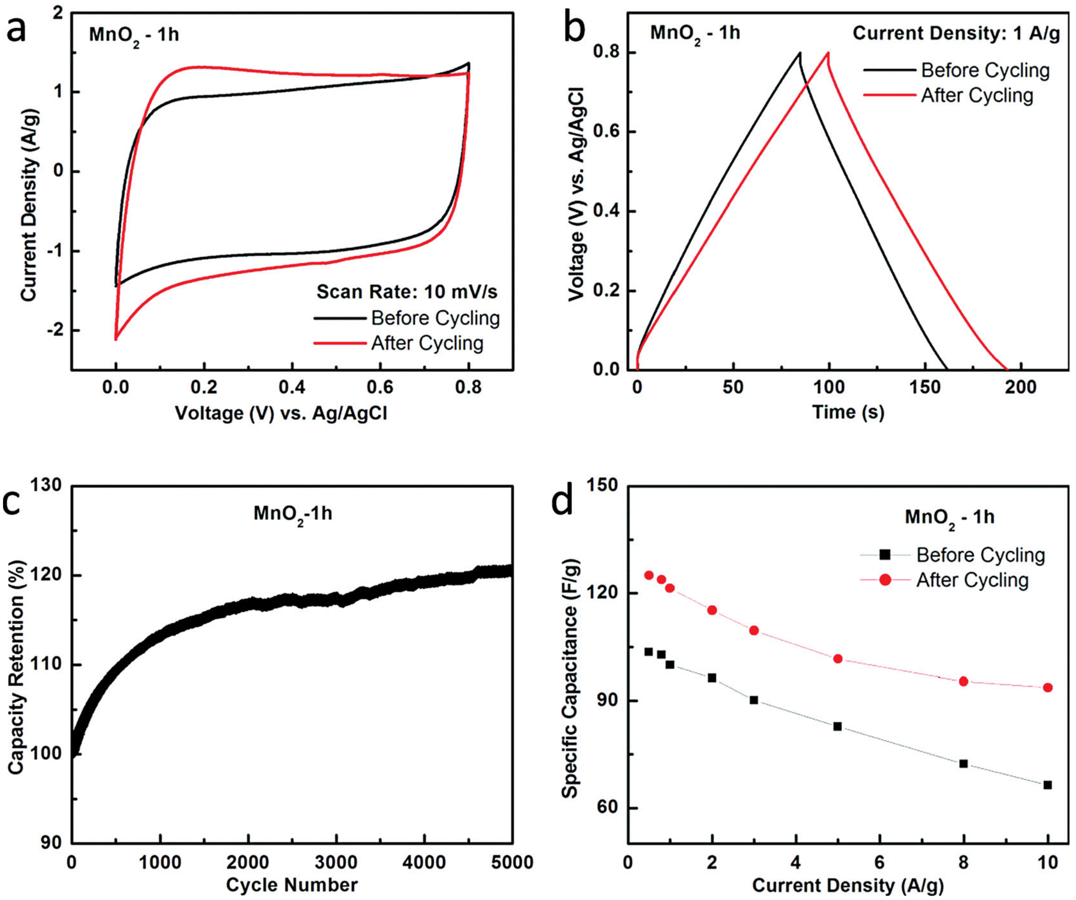

**Figure 8.** Comparison of electrochemical performance of $MnO_2$ nanospheres ($MnO_2$-1 h) as supercapacitor electrode materials before and after 5000 cycles. (a) Cyclic voltammetry at scan rate of 10 mV $s^{-1}$; (b) Galvanostatic charge-discharge at current density of 1 A $g^{-1}$; (c) The cycling stability over 5000 cycles; (d) The change of specific capacitance with current density.

are all displayed in Figure S4. It is interesting to note that the capacitance increases steadily during the 5000 cycles, showing a 20% increase after 5000 cycles (Figure 8c). The CV curves of the $MnO_2$-1 h sample also show that higher capacitance can be obtained after cycling test, as revealed by the larger CV loop area in Figure 8a. Similarly, the prolonged charge and discharge periods of the same sample indicate increased capacitance upon cycling (Figure 8b). The capacitance change with current density (Figure 8d) demonstrates that the specific capacitance increases with cycling over a range of current densities. A specific capacitance of 103.5 F $g^{-1}$ at current density of 0.5 A $g^{-1}$ is a typical value for $MnO_2$ prepared by the hydrothermal method.[22,36,37] The capacitance increase of about 20% after cycling at 1 A $g^{-1}$ is in good agreement with the cycling performance. Even at a high current density of 10 A $g^{-1}$, the capacitance of the sample after cycling is 93.7 F $g^{-1}$, which is higher than the value of 66 F $g^{-1}$ before cycling. The rate capability of the sample after cycling tests (a ratio of capacitance at 10 A $g^{-1}$ to 0.5 A $g^{-1}$) increased from 64% to 75%. EIS data shown in Figure S4e exhibits a lower equivalent series resistance after the cycling test, further demonstrating better electrochemical performance upon cycling.

All the $MnO_2$ samples after cycling tests exhibit excellent electrochemical properties in terms of rectangular shapes of CV curves (**Figure 9**a) and highly symmetrical CD curves (Figure 9b), which are similar to the behaviors of the samples before cycling tests. As summarized in Figure 9c, the specific capacitances after cycling are still highly dependent on the morphology and crystal phase of $MnO_2$. Additionally, the values of $MnO_2$-1 h and 1.5 h are still higher than that of the other samples. The specific capacitance of the $MnO_2$-1 h and 1.5 h increased to a range between 70 F $g^{-1}$ and 130 F $g^{-1}$, and the numbers of $MnO_2$-2 h, 4 h, 8 h and 12 h are in a range of 20 F $g^{-1}$ to 50 F $g^{-1}$. Further investigations demonstrate that the percentage increase of specific capacitance (the ratio of capacitance increase to the initial capacitance) of all the samples upon cycling is in the order of the hydrothermal reaction time. For example, the capacitance increased by about 20% for the sample of $MnO_2$-1 h after 5000 cycles (the value for $MnO_2$-1.5 h is 23.9%, $MnO_2$-2 h (39%), $MnO_2$-4 h (50.5%), $MnO_2$-8 h (65%)), while the increase rate for $MnO_2$-12 h is as high as 76%. Consequently, the specific capacitances of $MnO_2$ nanostructures have increased to a higher level upon cycling, depending on the specific morphology and crystal phase of the $MnO_2$ nanostructures. It is also found that the capacitance of $MnO_2$-1.5 h is close to that of $MnO_2$-1 h at low current densities and the capacitance values of $MnO_2$-2 h, 4 h, 8 h and 12 h are still almost in the same range after the cycling tests.

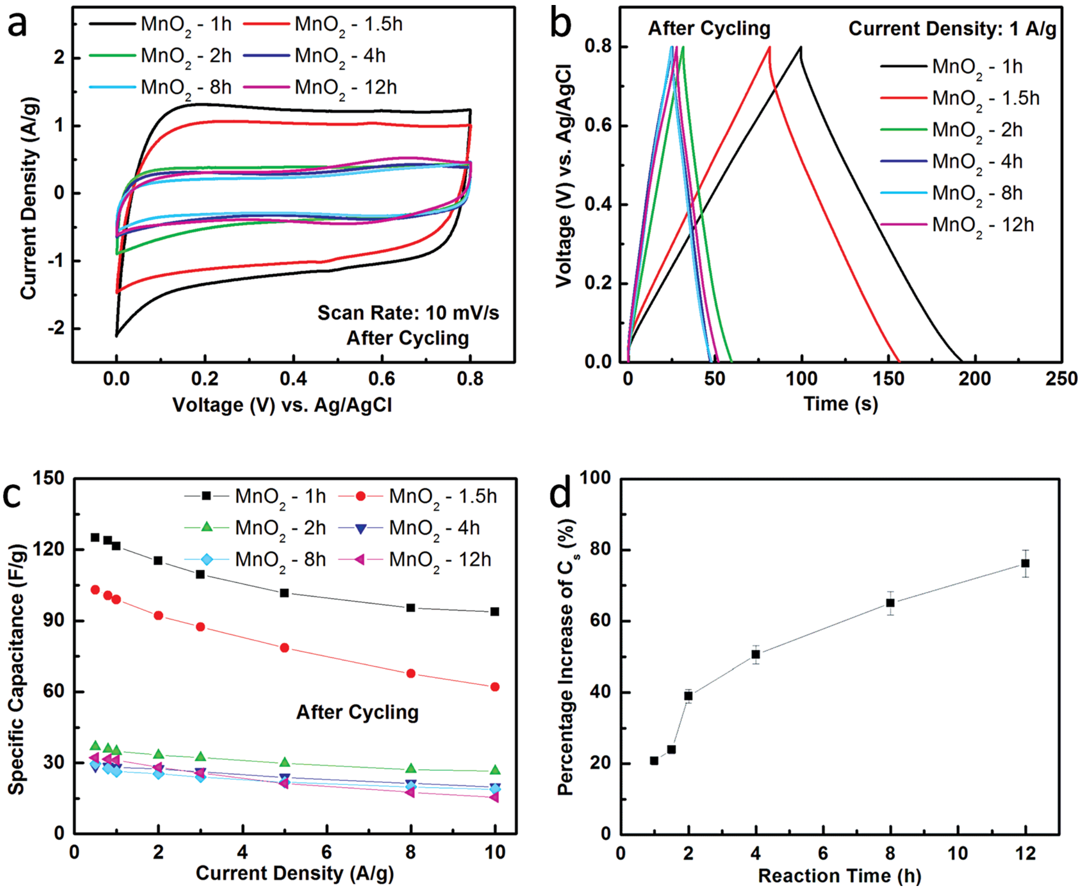

**Figure 9.** Electrochemical performance of all $MnO_2$ nanostructures as supercapacitor electrode materials after 5000 cycles. (a) Cyclic voltammetry at scan rate of 10 mV $s^{-1}$; (b) Galvanostatic charge-discharge curves at current density of 1 A $g^{-1}$; (c) Specific capacitance vs. current density; (d) The percentage increase of specific capacitance (0.5 $Ag^{-1}$) with the reaction time.

The Nyquist plots of all samples were compared separately before and after 5000 cycles, as shown respectively in Figure S11a and b. The $MnO_2$ samples show similar impedance behaviors before and after cycling tests. It is further demonstrated that the solution resistance of the $MnO_2$ electrodes increases with the reaction time in the preparation of $MnO_2$, where $MnO_2$-1 h sample shows the lowest solution resistance value while the $MnO_2$-12 h sample shows the highest one. This indicates that the $MnO_2$-1 h sample has higher ionic diffusion to the electrolyte than the other samples. However, the charge-transfer resistance of the $MnO_2$ electrode decreases with the sample preparation time, resulting in higher charge-transfer resistance of the $MnO_2$-1 h sample than that of $MnO_2$-12 h sample. This indicates that the electrochemical reaction on the interface of the $MnO_2$-12 h electrode and the electrolyte is the most facile, which is probably the reason that the $MnO_2$-12 h sample showed the highest capacitance increase among all the tested samples.

### 2.5. Mechanism of Capacity Change with Cycling

While the effects of morphology, crystal phase, and cycling on the supercapacitive performance of $MnO_2$ nanostructures have been reported previously, extensive analysis of the electrochemical perfromance-nanostructure correlation is still lacking.[22,38–41] Particularly, the reason of the commonly observed unusual increase in specific capacitance of the $MnO_2$ with cycling is still unknown so far.[39–41] We measured the electrochemical properties of the carbon paper that used as a current colletor in this study, which shows no capacity contribution to the $MnO_2$ electrodes, as demonstrated and discussed in Figure S12. In our study, we firstly conducted SEM and TEM studies to investigate any possible morphological or microstructural changes caused by the long term cycling tests. We focused on the samples with two extreme reaction times: $MnO_2$-1 h and $MnO_2$-12 h. Figure S13 shows the morphology of these two electrodes after 5000 cycles by SEM. It is interesting that the $MnO_2$ nanospheres on the electrode of $MnO_2$-1 h became highly porous after the cycling tests, while keeping their initial morphological features. Many “blooming nanoflowers” are deposited closely on the surface of the electrode, and the nanosheets of the $MnO_2$ nanospheres tend to face toward the electrode surface (Figure S13a). The gaps between the nanosheets of the $MnO_2$-1 h electrode after cycling tests became slightly larger (Figure S13b). These changes are probably caused by the repeated electrolyte ions insertion and extraction upon the

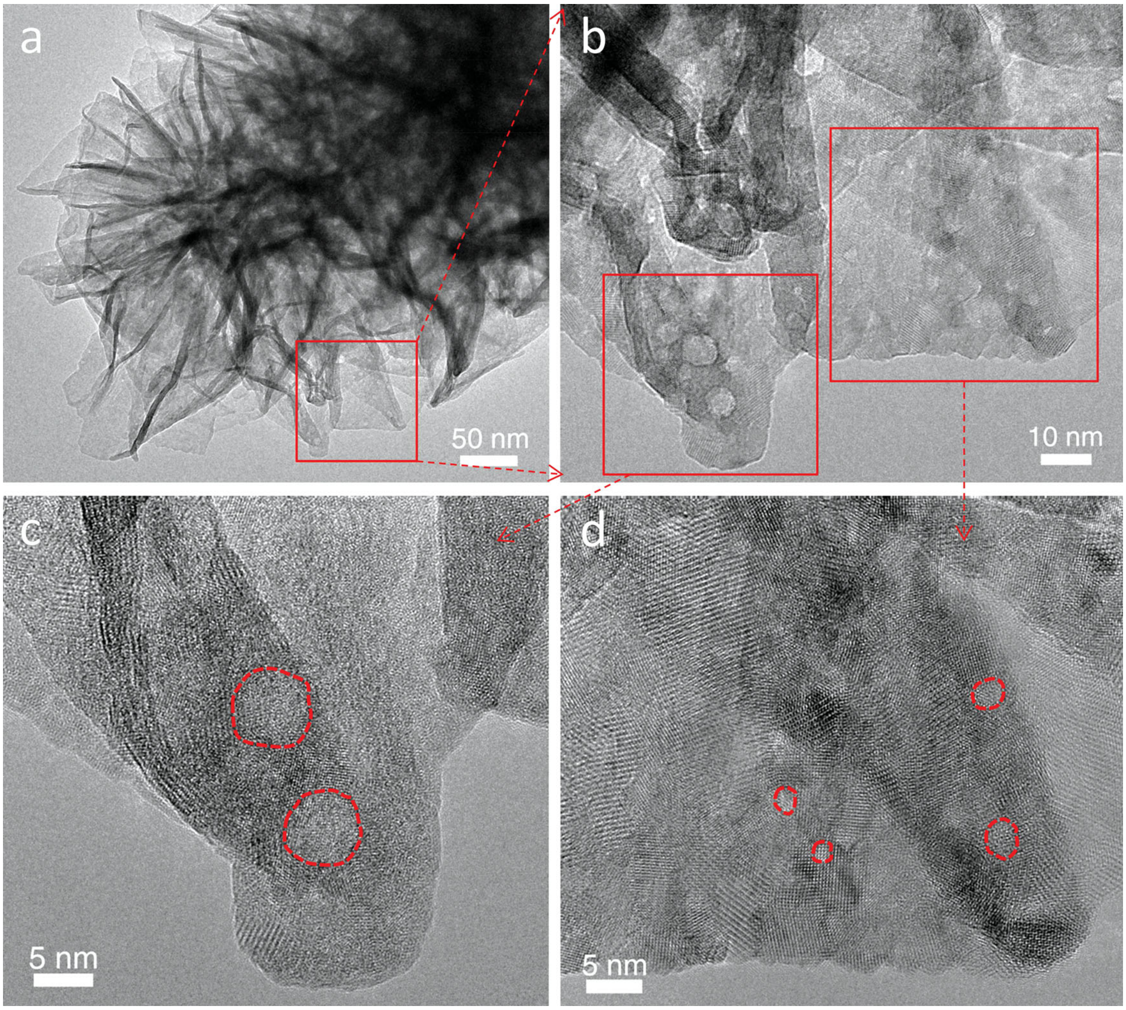

**Figure 10.** TEM images of $MnO_2$ nanoflowers ($MnO_2$-1 h) after 5000 cycling testes at different magnifications.

cycling tests. The nanosheets are forced to be vertical to the electrode surface in order to shorten the electrolyte ion transportation length, while the pores tend to become larger to facilitate more electrolyte accesses for ion adsorption/desorption or redox reactions between the electrode materials and electrolytes. However, the changes for the electrode of $MnO_2$-12 h upon cycling tests are not obvious from its SEM image (Figure S13c). $MnO_2$ nanotubes with random orientations are still heavily deposited on the surface of the electrode even after the cycling tests (Figure S13c,d). Therefore, it is necessary to employ TEM for the investigation of the microstructures. We are surprised to observe that many small defective or "disordered" regions are formed on some parts of the $MnO_2$ nanosheets (**Figure 10**) and nanotubes (**Figure 11**) after the cycling tests. As for the $MnO_2$ nanosheets ($MnO_2$-1 h), the materials generally kept their good porous feature and the folded nanosheets assembled to nanospheres (Figure 10a). Looking closely at some portions of the $MnO_2$ nanosheets (red square area in Figure 10a), we can see that some defective or disordered regions have been formed on the nanosheets (Figure 10b). This is totally different from the morphology of the smooth $MnO_2$ nanosheets before electrochemical cycling (Figure 3a and Figure 4a). The size of these regions, some of which may have become pores on the $MnO_2$ nanosheets, ranges from 2 nm to 7 nm, which is in the mesoporous range (2–50 nm). Enlarged view of the area with large sizes of the defective regions is shown in Figure 10c (left red square area in Figure 10b) indicates that the crystallinity of the regions became very poor as the lattice fringes tend to be disordered (labeled by the red circles). The defective regions with small sizes, shown in Figure 10d (right red square area in Figure 10b), demonstrate the disappearance of the crystalline fringes (labeled by the small red circles), similar to the change observed in the larger disordered regions in Figure 10c.

In the case of $MnO_2$ nanotube ($MnO_2$-12 h) after cycling tests, we found even more disordered regions are formed, making the whole nanotube highly porous (Figure 11a). Enlarged view of the tube in its central part (Figure 11b, the left red square area in Figure 11a) clearly shows a number of small defective sites throughout the whole tube. The size of the small defective or disordered regions is between 2 nm and 5 nm. The high resolution TEM image near the tip portion of the $MnO_2$ nanotube indicates that apart from the long gaps

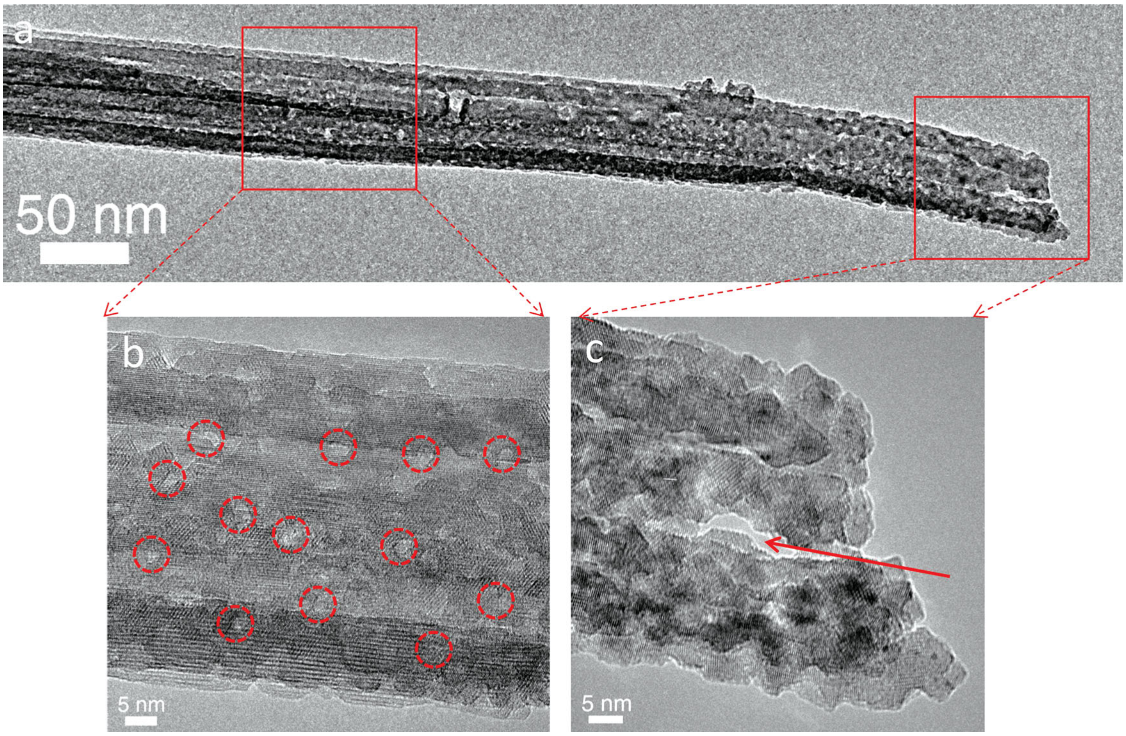

**Figure 11.** TEM images of $MnO_2$ nanotubes ($MnO_2$-12 h) after 5000 cycling testes at different magnifications.

formed in the hydrothermal process (labeled by the red arrow in Figure 11c), there are also small defective sites formed on the tube. It is worth pointing out that although some voids are formed on $MnO_2$ nanotubes during the hydrothermal reaction by the strong acid etching and ripening process, these voids are different in size and shape from the disordered regions formed after long-term electrochemical cycling tests. The similar results have been observed by Choi et al., where they found the formation and evolution of the nanopores in 1D nanostructures including Si nanowires, ZnO nanowires and Ag nanowires by means of lithium ion battery cycling tests.[42]

The formation of the defective regions within the $MnO_2$ nanostructures upon cycling is attributed to the repeated insertion/extraction of the electrolyte ions into/out of the $MnO_2$ electrode materials. The $Na^+$ ions from the electrolyte are expected to interact with $MnO_2$ on some active sites of the surface by either physisorption or fast and reversible redox reactions as shown in the following equation.

$$MnO_2 + xNa^+ + xe^- \leftrightarrow Na_xMnO_2 \qquad (3)$$

The porous structure induced by the electrochemical cycling tests contributes to the increase of the interaction due to the increased access of the electrolyte ions to the electrode materials. Hence the capacitance increases after electrochemical cycling tests. Due to the different $MnO_2$ electrode morphologies, the cycling-induced formation of defective/disordered regions differs from sample to sample. This fact results in varying degrees of capacitance increase after cycling (Figure 9d).

In order to identify the chemical and bonding states of the electrode material after cycling, we have conducted XPS analysis. As shown in **Figure 12**a, the prepared $MnO_2$ nanostructures are actually potassium doped $MnO_2$, which is introduced by $KMnO_4$ in the raw materials. The comparison between the $MnO_2$ samples before and after 5000 cycles clearly shows the appearance of the sodium peaks in the spectra for the sample after cycling tests, which indicates that Na interacts with the $MnO_2$ electrodes during cycling tests (Figure 12a). Quantitative analysis further reveals that the ratio of Na to Mn in the cycled electrode material is about 0.05. Therefore, we can denote the final compounds as $Na_{0.05}MnO_2$. The Mn 2p spectra exhibit characteristic peaks of Mn $2p_{3/2}$ (641.9 eV) and Mn $2p_{1/2}$ (653.5 eV), indicating the oxidation state is $Mn^{4+}$, which agrees well with the previous reports.[21] For the sample of $MnO_2$-1 h, no obvious changes of the Mn oxidation state can be observed from the Mn 2p spectra after the long term cycling, suggesting that the redox reaction between $MnO_2$ and the electrolyte is highly reversible and $MnO_2$ underwent no chemical changes after the cycling tests.

Based on the above observations, we can make the following conclusions to explain and enrich the electrochemical energy storage mechanism of $MnO_2$ in neutral $Na_2SO_4$ aqueous electrolyte in this study. Firstly, the $MnO_2$ electrode tends to become more porous during cycling due to repeated $Na^+$ insertion/extraction into/out of the electrode material. This effect enhances the porosity of the $MnO_2$ electrode and hence increases storage capacity during cycling. Secondly, the $MnO_2$ interacts with $Na^+$ to form Na doped $MnO_2$. However, only a small portion of the materials are involved in the interaction, giving limited doping level of the Na ions to the

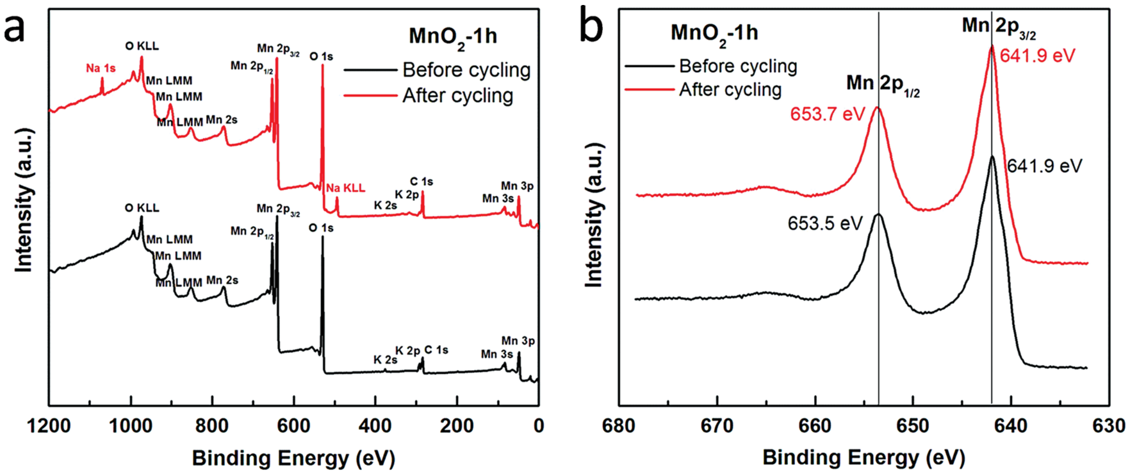

**Figure 12.** XPS of $MnO_2$ nanoflowers ($MnO_2$-1 h) before and after 5000 cycling testes. (a) Survey scan; (b) Mn 2p core level spectra.

$MnO_2$, indicating that only a thin layer of the $MnO_2$ electrode has contributed to the energy storage, and the $MnO_2$ undergoes no chemical changes after reaction. This is consistent with the energy storage mechanism of $MnO_2$ proposed earlier by Toupin et al.[21] Thirdly, the interaction of the $MnO_2$ with $Na^+$ introduced a high concetration of defective/disordered regions in some parts of $MnO_2$, further increasing the surface area and therefore the storage capacity of $MnO_2$.

## 3. Conclusions

We have reported a comprehensive study on the growth process, supercapacitor electrochemical performance, and cycling stability of hydrothermally-derived $MnO_2$ electrodes. It is proposed that the growth of different $MnO_2$ nanostructures is controlled by two steps: the conversion of $MnO_2$ nanosheets to nanofibers by a diffusion and crystallization process and the formation of $MnO_2$ nanotubes from nanofibers by a combined Ostwald ripening and acid etching processes. The morphological evolution of nanostructured $MnO_2$ was extensively studied and explained with the help of 3D electron tomography, revealing the vivid formation process from nanofibers to nanotubes. The electrochemical performance of $MnO_2$ supercapacitors was revealed to be highly correlated to their surface area, determined by their morphology and crystallinity, as well as their cycling performance, determined by their defective regions formation during cycling. The often observed unusual increase in specific capacitance with cycling was studied and correlated not only with $MnO_2$ electrode morphology, but also with its structural and chemical state, including the formation of defective regions on the materials and the interaction of the materials with the electrolyte. Our detailed study provides significant insight into the growth mechanism, electrochemical performance, and cycling behaviors of nanostructured $MnO_2$.

## 4. Experimental Section

*Materials*: All chemicals used in this study were purchased from Sigma Aldrich and used as received. Deionized water (18.2 MΩ·cm, Milli Q) was used throughout all experiments.

*Preparation of $MnO_2$ Nanostructures*: $MnO_2$ nanostructures with controlled morphologies were prepared from a facile hydrothermal route. In a typical procedure, $KMnO_4$ (0.263 g, 1.66 mmol) were dissolved in water (30 mL) with agitation at room temperature, followed by adding concentrated HCl (37%, 1 mL). After stirring for 5 min in air, the solution was transferred to a Teflon-lined stainless steel autoclave (capacity of 45 mL) and heated to 140 °C in an electric oven. In order to get designed morphology, the reaction of the solution was kept for different periods (1 h, 1.5 h, 2 h, 4 h, 8 h, 12 h), and the autoclave was then cooled naturally to room temperature. The resulting products were filtered, washed by water and absolute ethanol repeatedly to remove any possible residual reactants. Finally, the products were dried in an oven at 80 °C.

*Materials Characterization*: The microstructure and morphology of $MnO_2$ were characterized by SEM (Nova Nano 630, FEI), and TEM (T12 and Titan 80–300 kV (ST) TEM, FEI). The crystallographic structure of the samples was tested by XRD (D8 Advance bulk power XRD, Bruker). Surface area and pore size distribution measurement (ASAP 2420, surface area and pore size analyzer, Micromeritics) was carried out by nitrogen adsorption and desorption at bath temperature of –195.85 °C. The XPS analysis was conducted on a Kratos AXIS Ultra DLD spectrometer. A FEI Titan Super Twin 80-300 operated at 300 kV, equipped with a Fischione Dual-Axis tomography holder (Model 2040), was used to acquire the TEM images and STEM tomography tilt series. Fischione Annular Dark Field (ADF) detector (Model 3000) was used to acquire HAADF STEM images. The semi-convergence angle (alpha) of the probe is 10 mrad and HAADF STEM images was acquired at the detector inner and outer collection angles of 58 mrad and 200 mrad. The total data acquisition time was ~3 h which included the operation of tracking and focusing in manual mode. The tilt series were acquired at the range from –70 s to +70 degrees in Xplore 3D software (FEI Company) with the tilt increment of 2 degrees. Inspect3D software (FEI Company) was used to process the tilt series using a cross correlation method for image shift and tilt alignments, and the 3D reconstruction was performed by simultaneous iterative reconstruction technique (SIRT) with 30 iterations. The visualization of the 3D datasets was performed by using isosurface and volume rendering in Avizo Fire software.

*Electrochemical Measurements*: All electrochemical tests in this study were conducted at room temperature in a three-electrode configuration, with Pt wire used as counter electrode, Ag/AgCl as reference electrode, and $MnO_2$ coated on carbon paper as working electrode. $MnO_2$ with different morphologies acting as active material was each mixed with acetylene black and polytetrafluoroethylene (PTFE) binder with a ratio of 80:10:10 in ethanol to form homogenous electrode slurry. The electrodes of supercapacitors were prepared by drop casting of the slurry onto graphitized carbon papers. Then the electrodes were vacuum dried at 100 °C for 12 h. The mass of the materials on the electrode was determined by a microbalance (Mettler Toledo XP26, resolution of 1 μg) using the mass difference before and after materials loading. The typical mass loading of the electrodes is 2~3 mg cm$^{-2}$. The electrolyte used in this study is 1 M $Na_2SO_4$. The electrochemical performance was tested in a VMP3 multi-channel electrochemical workstation (Bio-Logic) by the techniques of electrochemical impedance spectroscopy (EIS), cyclic voltammetry (CV) and galvanostatic charge-discharge (CD). The EIS was measured with frequency range between 100 kHz and 100 mHz. The CV was tested from scan rate of 5 mV s$^{-1}$ to 100 mV s$^{-1}$ with voltage window from 0 to 0.8 V vs. Ag/AgCl. The CD measurement was conducted from current density of 0.5 A g$^{-1}$ to 10 A g$^{-1}$ with the same voltage window as the CV tests. The capacitance values were calculated from galvanostatic charge-discharge curves according to our previous reports.[43,44] The galvanostatic charge and discharge technique was used to determine the cycling performance for all samples: current density of 5 A/g for the sample of $MnO_2$-1 h, 3 A/g for the sample of 1.5 h, and 1 A/g for the samples of $MnO_2$-2 h, 4 h, 8 h and 12 h, ensuring that the initial charge–discharge can be finished within ~30 s.

## Supporting Information

Supporting Information is available from the Wiley Online Library or from the author.

## Acknowledgements

The authors thank for the characterization facilities provided by KAUST Advanced Imaging and Characterization Laboratory and Analytic Core Laboratory. We acknowledge the help from Olga Zausalina for the illustration drawing. W.C. acknowledges KAUST Graduate Fellowship. R.B.R. acknowledges SABIC Postdoctoral Fellowship, and H.N.A. acknowledges support from the KAUST baseline fund.

Received: October 13, 2013
Revised: November 29, 2013
Published online: February 12, 2014

---

[1] M. M. Thackeray, *Prog. Solid State Chem.* **1997**, *25*, 1.
[2] F. Cheng, J. Zhao, W. Song, C. Li, H. Ma, J. Chen, P. Shen, *Inorg. Chem.* **2006**, *45*, 2038.
[3] A. Débart, A. J. Paterson, J. Bao, P. G. Bruce, *Angew. Chem. Int. Ed.* **2008**, *47*, 4521.
[4] M. Toupin, T. Brousse, D. Bélanger, *Chem. Mater.* **2002**, *14*, 3946.
[5] W. F. Wei, X. W. Cui, W. X. Chen, D. G. Ivey, *Chem. Soc. Rev.* **2011**, *40*, 1697.
[6] J. R. Miller, P. Simon, *Science* **2008**, *321*, 651.
[7] P. Simon, Y. Gogotsi, *Nat. Mater.* **2008**, *7*, 845.
[8] A. S. Arico, P. Bruce, B. Scrosati, J. M. Tarascon, W. Van Schalkwijk, *Nat. Mater.* **2005**, *4*, 366.
[9] X. Wang, A. Yuan, Y. Wang, *J. Power Sources* **2007**, *172*, 1007.
[10] T. Brousse, M. Toupin, R. Dugas, L. Athouël, O. Crosnier, D. Bélanger, *J. Electrochem. Soc.* **2006**, *153*, A2171.
[11] W. N. Li, J. Yuan, X. F. Shen, S. Gomez-Mower, L. P. Xu, S. Sithambaram, M. Aindow, S. L. Suib, *Adv. Funct. Mater.* **2006**, *16*, 1247.
[12] L. Hu, W. Chen, X. Xie, N. Liu, Y. Yang, H. Wu, Y. Yao, M. Pasta, H. N. Alshareef, Y. Cui, *ACS Nano* **2011**, *5*, 8904.
[13] Z. Yu, B. Duong, D. Abbitt, J. Thomas, *Adv. Mater.* **2013**, *25*, 3302.
[14] C. Yang, M. Zhou, Q. Xu, *Phys. Chem. Chem. Phys.* **2013**, *15*, 19730.
[15] J. Zhao, Z. Tao, J. Liang, J. Chen, *Crystal Growth Des.* **2008**, *8*, 2799.
[16] W. Xiao, D. Wang, X. W. Lou, *J. Phys. Chem. C* **2009**, *114*, 1694.
[17] X. Wang, Y. Li, *J. Am. Chem. Soc.* **2002**, *124*, 2880.
[18] F. Cheng, Y. Su, J. Liang, Z. Tao, J. Chen, *Chem. Mater.* **2009**, *22*, 898.
[19] T. T. Truong, Y. Liu, Y. Ren, L. Trahey, Y. Sun, *ACS Nano* **2012**, *6*, 8067.
[20] J. Ni, W. Lu, L. Zhang, B. Yue, X. Shang, Y. Lv, *J. Phys. Chem. C* **2008**, *113*, 54.
[21] M. Toupin, T. Brousse, D. Bélanger, *Chem. Mater.* **2004**, *16*, 3184.
[22] V. Subramanian, H. Zhu, R. Vajtai, P. M. Ajayan, B. Wei, *J. Phys. Chem. B* **2005**, *109*, 20207.
[23] M. Yeager, W. Du, R. Si, D. Su, N. Marinković, X. Teng, *J. Phys. Chem. C* **2012**, *116*, 20173.
[24] J. Luo, H. T. Zhu, H. M. Fan, J. K. Liang, H. L. Shi, G. H. Rao, J. B. Li, Z. M. Du, Z. X. Shen, *J. Phys. Chem. C* **2008**, *112*, 12594.
[25] S. J. Pennycook, P. D. Nellist, *Scanning Transmission Electron Microscopy Imaging and Analysis*, Springer, New York, USA **2011**.
[26] P. A. Midgley, R. E. Dunin-Borkowski, *Nat. Mater.* **2009**, *8*, 271.
[27] X. Wang, Y. Li, *Chem. Eur. J.* **2003**, *9*, 300.
[28] Y. Li, J. Wang, Y. Zhang, M. N. Banis, J. Liu, D. Geng, R. Li, X. Sun, *J. Colloid Interface Sci.* **2012**, *369*, 123.
[29] Y.-T. Wang, A.-H. Lu, H.-L. Zhang, W.-C. Li, *J. Phys. Chem. C* **2011**, *115*, 5413.
[30] R. B. Rakhi, D. Cha, W. Chen, H. N. Alshareef, *J. Phys. Chem. C* **2011**, *115*, 14392.
[31] J. Chmiola, G. Yushin, R. Dash, Y. Gogotsi, *J. Power Sources* **2006**, *158*, 765.
[32] A. J. Roberts, R. C. T. Slade, *Electrochim. Acta* **2010**, *55*, 7460.
[33] S. W. Lee, J. Kim, S. Chen, P. T. Hammond, Y. Shao-Horn, *ACS Nano* **2010**, *4*, 3889.
[34] S.-B. Ma, K.-Y. Ahn, E.-S. Lee, K.-H. Oh, K.-B. Kim, *Carbon* **2007**, *45*, 375.
[35] L. Bao, J. Zang, X. Li, *Nano Lett.* **2011**, *11*, 1215.
[36] M. Xu, L. Kong, W. Zhou, H. Li, *J. Phys. Chem. C* **2007**, *111*, 19141.
[37] P. Yu, X. Zhang, D. Wang, L. Wang, Y. Ma, *Crystal Growth Des.* **2008**, *9*, 528.
[38] S. Devaraj, N. Munichandraiah, *J. Phys. Chem. C* **2008**, *112*, 4406.
[39] L. Athouel, F. Moser, R. Dugas, O. Crosnier, D. Belanger, T. Brousse, *J. Phys. Chem. C* **2008**, *112*, 7270.
[40] D.-Y. Sung, I. Y. Kim, T. W. Kim, M.-S. Song, S.-J. Hwang, *J. Phys. Chem. C* **2011**, *115*, 13171.
[41] O. Ghodbane, J.-L. Pascal, F. d. r. Favier, *ACS Appl. Mater. Interfaces* **2009**, *1*, 1130.
[42] J. W. Choi, J. McDonough, S. Jeong, J. S. Yoo, C. K. Chan, Y. Cui, *Nano Lett.* **2010**, *10*, 1409.
[43] W. Chen, R. B. Rakhi, L. Hu, X. Xie, Y. Cui, H. N. Alshareef, *Nano Lett.* **2011**, *11*, 5165.
[44] W. Chen, R. B. Rakhi, H. N. Alshareef, *Nanoscale* **2013**, *5*, 4134.